Research Article | Vol. 29, No. 11 / 24 May 2021 / Optics Express 17227
Optics EXPRESS

# Automated freeform imaging system design with generalized ray tracing and simultaneous multi-surface analytic calculation

YUNFENG NIE,[1,*] DAVID R. SHAFER,[2] HEIDI OTTEVAERE,[1] HUGO THIENPONT,[1] AND FABIAN DUERR[1]

[1]Brussels Photonics Team, Department of Applied Physics and Photonics, Vrije Universiteit Brussel, Pleinlaan 2, B-1050 Brussels, Belgium
[2]David Shafer Optical Design, 56 Drake Lane, Fairfield, CT. 06824, USA
[*]Yunfeng.Nie@vub.be

**Abstract:** Recently, freeform optics has been widely used due to its unprecedented compactness and high performance, especially in the reflective designs for broad-wavelength imaging applications. Here, we present a generalized differentiable ray tracing approach suitable for most optical surfaces. The established automated freeform design framework simultaneously calculates multi-surface coefficients with merely the system geometry known, very fast for generating abundant feasible starting points. In addition, we provide a "double-pass surface" strategy with desired overlap (not mutually centered) that enables a component reduction for very compact yet high-performing designs. The effectiveness of the method is firstly demonstrated by designing a wide field-of-view, fast f-number, four-mirror freeform telescope. Another example shows a two-freeform, three-mirror, four-reflection design with high compactness and cost-friendly considerations with a double-pass spherical mirror. The present work provides a robust design scheme for reflective freeform imaging systems in general, and it unlocks a series of new 'double-pass surface' designs for very compact, high-performing freeform imaging systems.



## 1. Introduction

Growing interest in freeform optics is fostered by the rapid advances in precise fabrication techniques and replica of optical components with almost any shape [1–3]. Including freeform components in optical systems provides numerous opportunities for unprecedented performance and lightweight, compact packaging, which has already been proven in various applications, such as telescopes [4,5], spectrometer [6], Augmented Reality (AR) [7], beam shaping [8] and tailored illuminations [9,10]. Many optical design processes are still largely dependent on time-consuming and often tedious 'initial guess - iterative optimizations' loops to achieve a qualified result. However, this routine design strategy has been challenged by freeform optical systems due to the many more freedoms of degree to accurately describe such surfaces and the limited availability of adequate, feasible initial designs.

The optical design community is joining forces to overcome the issues regarding freeform imaging system design [11]. Various mainstream approaches have been proposed, to name a few, (i) paraxial design with commercial software optimization [7,12], (ii) nodal aberration theory [13,14], (iii) automated design with advanced optimization [15,16] and (iv) direct design with certain aberrations vanished [17–19]. The first design strategy relies on a good starting point which is usually from a paraxial calculation of classic aberration theories, and then generalizes a sophisticated merit function by using commercial optical design software (e.g. Zemax or Code V) for iterative optimization. This method can target different features of freeform optics, for example, applying orthogonal surface representations to ease manufacturability or increase the optimization speed [20,21]. However, practical issues such as deviations from best fitting

#426207 https://doi.org/10.1364/OE.426207
Journal © 2021 Received 25 Mar 2021; revised 10 May 2021; accepted 11 May 2021; published 19 May 2021

Optics EXPRESS

sphere (BFS), frequent occurrences of obscuration and overall volume are usually ignored by default merit functions. Noting that the paraxial assumptions have been made for raytracing among most optical design software, while the usage of freeform surfaces usually violates this assumption which leads to unreliable calculations of crucial metrics like effective focal length (EFL) and distortions. Secondly, the nodal aberration theory provides an insightful and systematic evaluation of different surface Zernike terms to full-field aberration corrections [22,23], which need profound optical design skills and not readily to use for novice optical designers. In contrast, the third automatic design strategy is more brute-force but quite practical, which is usually a point-to-point construction process to minimize a user-defined merit function for a high overall imaging performance [15]. Due to the considerable surface fitting for continuously increased point clouds, the process can be time-consuming. The fourth design strategy starts from more fundamental optical laws (e.g. Fermat's law) to cancel desired aberrations to certain order, thus called direct design. This strategy was known for N optical surfaces to achieve N perfect imaging points of lens design in the beginning, and later extended to more surfaces and off-axis mirrors [18,24–26].

While freeform imaging designs with three mirrors are omnipresent with all the above-mentioned methods, high-performing four-mirror freeform designs are rarely reported in literature. It is possible that such methods are not yet fully adapted to the increased complexity in solution space. Besides, one additional freeform component largely arises fabrication and assembly costs, which might cancel the benefits of a faster F-number and a larger field-of-view (FOV) brought by a four-mirror design. Efforts have been made to directly construct four-mirror anastigmatic spherical/conic designs [27–30], which can be further optimized as freeform systems. However, they are usually limited to slow F-number and small FOV [31]. Last but not least, complex freeform optical design is 'notorious' that the same design is hardly reproducible without an exact recipe on each step, while such data is usually very difficult to archive.

Here, we tackle these problems with our developed freeform optical design framework. In this method, an exact set of freeform surface parameters is solved for each design with merely the initial mirror and detector positions as input parameters, thus an initial (hand-picked) geometry can always converge to an improved starting design with most aberrations corrected in a few minutes. All the processing time in this work is based on a single-CPU laptop (Intel i7-8850H CPU, 16GB RAM), and a high-performance computing workstation is not required. In the following sections, we firstly present the fundamentals of the proposed method. Then, a wide FOV, fast f-number, four-mirror freeform imaging system is designed with comparable performance to a state-of-the-art design. Furthermore, we propose the 'double-pass surface' strategy to generate a novel class of two-freeform, three-mirror, four-reflection designs, leading to an excellent imaging performance with more compact packaging and reduced manufacturing, assembly complexity. The main contributions of this work are summarized as follows: (1) we generalize a differentiable raytracing approach that leads to rapid 'first time right' designs by calculating multiple surface coefficients simultaneously; (2) we provide versatile user-defined metrics and a variable stop surface to realize a very flexible freeform optimization process targeting different priorities, e.g. image quality or manufacturability; and (3) a new series of folded freeform imaging designs with the proposed 'double-pass surface' strategy is presented, enabling reduced components and super-compact packaging with high image quality.

## 2. Fundamentals and design method

The proposed design framework consists of three modules: the input, the processing and the output, as summarized in the flowchart (Fig. 1). The input parameters are the system specifications, namely the effective focal length (EFL, can differ in x- and y-direction), the field of view (FOV, optionally circular or rectangular), the F-number (or the entrance pupil diameter, ENPD), an optional stop surface # and an optional parameter to indicate if the 'double-pass

Optics EXPRESS

surface' strategy is used or not, as well as the system geometry indicated by surface positions or distances plus angles. After the input parameters are given, they are sent to the 'first-time-right' calculation where the necessary information to generate all the metrics are calculated directly and rapidly. Then an optimization algorithm is performed based on the selected metrics, noting that the system geometry parameters (e.g. surface positions) are variables to allow obscuration removal. When the stop criteria are met, the system and surface parameters are given to further check the image quality, manufacturability, and system volume, etc. This step can be done in our developed program or by importing the output system parameters to a commercial optical design software. More details are given below.

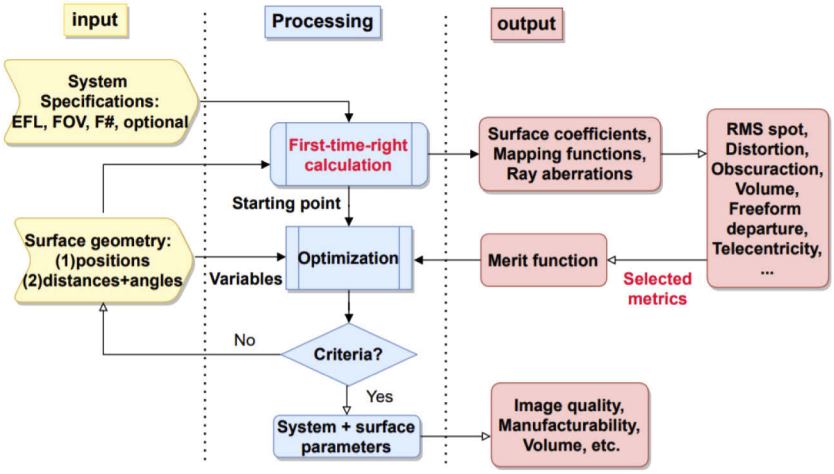


**Fig. 1.** Flowchart of the propose design framework, which highlights the minimal required input by the user, and the wide range of directly calculated coefficients and metrics

### 2.1. Generalized freeform ray tracing

The system coordinate definitions are generic to any reflective imaging system. As an example, a schematic four-mirror design is used to describe the notations as seen in Fig. 2. The surface positions of the four freeform mirrors M1-M4 and the image plane M5 are defined in a global coordinate system **XYZ**, denoted by their vertices $P_{Mi}$ ($X_i$, $Y_i$, $Z_i$). Each surface geometry is described by its local coordinate **uvf**. The surface sag functions $f_i(u_i, v_i)$ are defined locally with their origins on the vertices $p_i(u_i, v_i, f_i)$. Like any imaging system, the ray tracing starts from an entrance pupil with a certain ray sampling pattern. The origin of the global coordinate is placed at the center of the entrance pupil, while the pupil stop could be positioned at any surface of the system.

One ray is regarded as emitting from one point on the object plane to another point on the entrance pupil. On the object plane, one object point emitting a bundle of rays is one field, described by a normalized 2D position or angular vector ($h_x$, $h_y$) when the object is from finite distances or infinity respectively. The proposed method is applicable for both situations, while in this context will focus only on objects from infinity if not specified otherwise. On the entrance pupil, we sample the circular area by a certain pattern, e.g. Gaussian quadrature with certain rings and arms [32], and each point is denoted by a normalized 2D-vector ($p_x$, $p_y$). Any ray entering the imaging system is solely determined by a 4D-vector ($p_x$, $h_x$, $h_y$), denoted as 4D ray.

Let us consider a sequence of N reflective optical surfaces $s_i$ ($i$=1...N) aligned along the on-axis chief ray path. Once the surface positions are known, the surface tilts $\theta_i$ and distances $d_i$ between two adjacent surfaces are readily calculated to make the chief ray go through each mirror

Optics EXPRESS

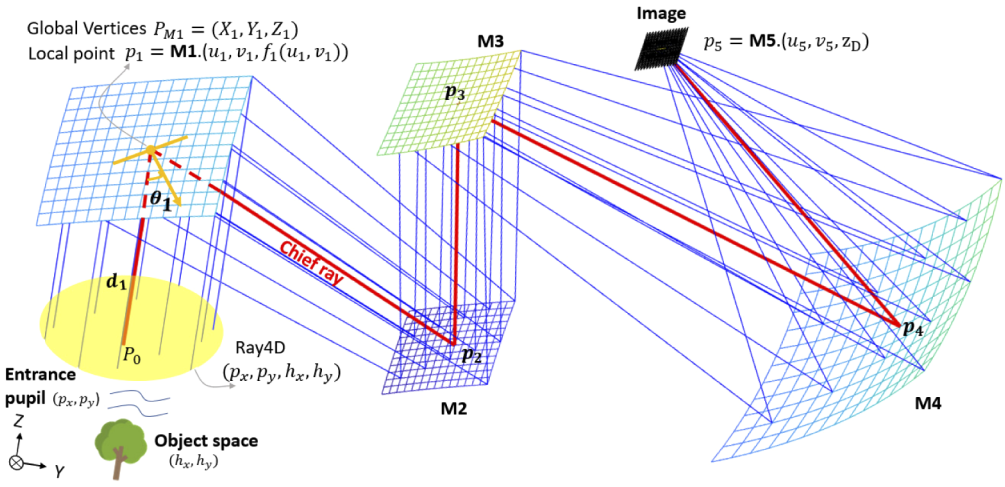


**Fig. 2.** Generalized ray tracing of an unobscured four-mirror imaging system that propagates a bundle of 4D rays via the mapping of the pupil grid on each surface

center and reach the detector center, more details are seen in Supplement 1. The generalized ray tracing allows a bundle of 4D rays propagate through surfaces by grid as seen in Fig. 2. The mapping functions $u_i, v_i$ record the trajectories of the 4D ray grid by mapping them from entrance pupil to image plane (denote as N+1), which are represented in power series

$$u_i\left(p_x, p_y, h_x, h_y\right) = \sum_{j=0}^{J}\sum_{k=0}^{K}\sum_{l=0}^{L}\sum_{m=0}^{M} \bar{u}_{i,\,jklm} p_x^j p_y^k h_x^l h_y^m, \quad i = 1 \ldots \mathrm{N{+}1}, \tag{1}$$

$$v_i(p_x, p_y, h_x, h_y) = \sum_{j=0}^{J}\sum_{k=0}^{K}\sum_{l=0}^{L}\sum_{m=0}^{M} \bar{v}_{i,\,jklm} p_x^j p_y^k h_x^l h_y^m, \quad i = 1 \ldots \mathrm{N}+1. \tag{2}$$

The surface functions are also denoted as the power series in local coordinates $(u_i, v_i)$

$$f_i(u_i, v_i) = \sum_{s=0}^{S}\sum_{t=0}^{T} \bar{f}_{i,st} u_i^{\,s} v_i^{\,t}, \; i = 1 \ldots \mathrm{N}, \tag{3a}$$

where, j, k, l and m denote the orders of normalized pupil coordinate and field coordinate. $\bar{u}_{i,jklm}$, $\bar{v}_{i,jklm}$, $\bar{f}_{i,st}$ are mapping coefficients and $\bar{f}_{i,st}$ are surface coefficients. Among many surface expressions, power series are used in this work due to their infinitely differentiable feature and the associated benefits in solving following high-order partial differential equations [33]. If all these coefficients are solved, then all the freeform surfaces are determined.

Normally, a N-reflection design results in N separate mirrors. However, less components can form a more compact packaging as well as greatly ease the fabrication and assembly procedures. In viewing of this, a double-pass surface strategy is readily to be implemented in this generalized ray tracing module. As for a N-reflection (N>=4) initial geometry, we can force two non-adjacent mirrors to have the same global coordinates and surface coefficients, e.g. $P_{Mi} = P_{Mi+2}, \bar{f}_{i,st} = \bar{f}_{i+2,st}$, $(i = 1, 2, ..)$. Therefore, a 'double-pass surface' is generated with a few additional constraint equations, which will narrow the solution space, but it does not break the generality of the proposed method. Further implementation of the 'double-pass surface' strategy is explained in Sec 3.2.

With respect to manufacturing, we can separate the spherical part and the high-order terms in Eq. (3a) to better visualize the freeform departure. As the expression of power series is close to XY polynomials, a widely used freeform surface type is adopted, which is mathematically

Optics EXPRESS

represented by a spherical basis and the freeform departure portion

$$f_i(x,y) = \frac{c_i(x^2+y^2)}{1+\sqrt{1-c_i^2(x^2+y^2)}} + \sum_{m=0}^{M}\sum_{n=0}^{N} A_{i,mn}x^m y^n,\ i = 1\ldots \mathrm{N}. \tag{3b}$$

where, $c_i$ is the paraxial curvature of the surface, $A_{i,mn}$ are corresponding coefficients of the polynomial terms. Given the YZ-plane symmetry, only even x-terms are used. The calculated freeform surface coefficients from Eq. (3a) are easily converted to Eq. (3b) for characterizing the freeform departure from best fitting sphere (BFS). In principle, once the coefficients $\bar{f}_{i,st}$ are known, the surface type can be converted to most well-known freeform surface types, e.g. Zernike polynomials [21], Forbes Q polynomials [20] and alike.

Based on focal length definition, each ideal image point is calculated by

$$u_{ideal} = F_x\ .\ \tan(h_x) \text{ and } v_{ideal} = F_y\ .\ \tan(h_y),\ \text{for infinite object.} \tag{4}$$

where, $F_x$ and $F_y$ are the focal lengths in X- and Y-direction respectively. The magnification and object height are used if the object is from finite.

The transverse ray aberrations are the X- and Y- deviations of arbitrary ray from its ideal image point, which we also write in ascending power series as $\epsilon^{(o)} = (\epsilon_x, \epsilon_y)$

$$\epsilon_x(p_x,p_y,h_x,h_y) = u_{N+1} - u_{ideal} = \sum_{j=0}^{J}\sum_{k=0}^{K}\sum_{l=0}^{L}\sum_{m=0}^{M} \bar{\epsilon}_{x,\,jklm} p_x^j p_y^k h_x^l h_y^m, \tag{5}$$

$$\epsilon_y(p_x,p_y,h_x,h_y) = v_{N+1} - v_{ideal} = \sum_{j=0}^{J}\sum_{k=0}^{K}\sum_{l=0}^{L}\sum_{m=0}^{M} \bar{\epsilon}_{y,\,jklm} p_x^j p_y^k h_x^l h_y^m. \tag{6}$$

where, $o = j + k + l + m$ denotes the corresponding aberration order to be corrected.

With the Eqs. (1)–(6), a generalized raytracing method is presented which is applied to most types of optical surfaces (spherical, aspherical, and freeform) since they can all be well described by the power series in Eq. (3a). It is important to point out that, this generalization provides a differentiable raytracing suitable for other optimization strategies, and it closely links with all fields and the entire pupil to target different system specifications.

### 2.2. Analytic 'first time right' multi-surface calculation

Analytic calculation of freeform coefficients has been demonstrated by many cases in both non-imaging and imaging lens systems [34,35]. Recently, the method is further extended to deal with both catoptric and/or dioptric optical surfaces [36]. In this work, we further develop the design method for multiple surfaces up to 4$^{\text{th}}$. This process allows to calculate the above-mentioned surface, mapping, and aberration coefficients, which offers 'first time right' initial imaging systems for a given geometry. In that sense, it provides a local and deterministic solution rather than a global solution.

To ensure the first-order feature of the design and cancel the residual transverse aberrations $\epsilon^{(o)}$ from Eqs. (5) and (6), we assume a ray path from object to image plane that consists of (N+1) segments with corresponding distances $d_1 \ldots d_{N+1}$, as seen in Fig. 2. Fermat's principle implies that

$$\boldsymbol{D_{i,x}} = \partial_{u_i}(\boldsymbol{d_i} + \boldsymbol{d_{i+1}}) = 0,\ \boldsymbol{i = 1\ldots N}, \tag{7}$$

$$\boldsymbol{D_{i,y}} = \partial_{v_i}(\boldsymbol{d_i} + \boldsymbol{d_{i+1}}) = 0,\ \boldsymbol{i = 1\ldots N}. \tag{8}$$

where, $d_{i+1}$ is the Euclidean norm of point $p_i$ to $p_{i+1}$. If refractive surfaces are used, the optical path lengths are given by $n_i d_i$, with the refractive index $n_i$ at a certain design wavelength. An optical system consisting of N optical surfaces is fully described by these 2N partial differential equations $\boldsymbol{D_{i,x}}$ and $\boldsymbol{D_{i,y}}$. Thus, we obtain $\mathrm{D_{4,x}} = (\mathrm{u_4}, \mathrm{v_4},\ \mathrm{f(u_4, v_4)}) - (\mathrm{u_3}, \mathrm{v_3},\ \mathrm{f(u_3, v_3)}) + (\mathrm{u_5},\ \mathrm{v_5}, \mathrm{z_D}) - (\mathrm{u_4}, \mathrm{v_4},\ \mathrm{f(u_4, v_4)})$

Optics EXPRESS

when $i$=4. If the condition of Eq. (4) is fully implemented in this optical path calculation, the focal length and other first-order related properties are ensured. Furthermore, different focal lengths in X- and Y- directions are allowed.

To calculate those unknown coefficients $\bar{u}_{i,jklm}$, $\bar{v}_{i,jklm}$, $\bar{f}_{i,st}$ from Eqs. (1)–(3), we differentiate Eqs. (7) and (8) with respect to $p_x, p_y, h_x, h_y$ in different aberration orders and evaluate at $p_x = p_y = h_x = h_y = 0$ as follows

$$\lim_{p_x\to 0} lim_{\,p_y\to 0}\, lim_{\,h_x\to 0}\, lim_{\,h_y\to 0}\ \frac{\partial^j}{\partial p_x^j}\frac{\partial^k}{\partial p_y^k}\frac{\partial^l}{\partial h_x^l}\frac{\partial^m}{\partial h_y^m} D_{i,x} = 0,\ i = 1\ldots N, \tag{9}$$

$$\lim_{p_x\to 0} lim_{\,p_y\to 0}\, lim_{\,h_x\to 0}\, lim_{\,h_y\to 0}\ \frac{\partial^j}{\partial p_x^j}\frac{\partial^k}{\partial p_y^k}\frac{\partial^l}{\partial h_x^l}\frac{\partial^m}{\partial h_y^m} D_{i,y} = 0,\ i = 1\ldots N. \tag{10}$$

where, $D_{i,x}$ and $D_{i,y}$ are functions of $u_i$, $v_i$, $\epsilon_x$, $\epsilon_y$ and $f_i$. According to the definitions of them in Eqs. (1)–(6), these functions are all analytic, smooth, and infinitely differentiable.

With the underlying differential equations established, as well as the overall system specifications (EFL, ENPD, FOV) and geometry (determined by the surface positions or surface distances plus tilts), the 'first time right' calculation process is performed by solving the derived differential Eqs. (9) and (10) in ascending orders sequentially.

(1) When j=k=l=m=0 for the zero-order case, we substitute Eqs. (7) and (8) into the differential Eqs. (9) and (10). The initial values of this equation set are automatically fulfilled as they are mathematically equivalent to the defined optical path of the chief ray $P_{M1} \to P_{M2} \ldots \to P_{M5}$.

(2) When o=j+k+l+m=1, we derive the first-order case for all (j,k,l,m) combinations given Eqs. (9) and (10), which results in a set of nonlinear equations for the second-order surface coefficients $\bar{f}_{i,st}$ (s+t=2), the first-order mapping coefficients $\bar{u}_{i,jklm}$ (i + l = 1) and $\bar{v}_{i,jklm}$ (k + m = 1), the aberration coefficients ($\bar{\epsilon}_{x,\,1,0,0,0}$, $\bar{\epsilon}_{x,\,0,0,1,0}$, $\bar{\epsilon}_{y,\,0,1,0,1}$, $\bar{\epsilon}_{y,\,0,0,0,1}$). Setting the latter four aberrations coefficients to zero or minimizing them to calculate the unknown surface coefficients $\bar{f}_{i,st}$ and first-order mapping coefficients. Extra conditions for the second order surface coefficients can be imposed if desired. We can solve them either by using a user-defined non-linear solver or by making use of alternative matrix optics tools [30].

(3) For each higher order **o**=j+k+l+m=2,3..., we can derive the exact linear relationship among the surface, mapping and aberration coefficients for all corresponding indices (i,j,k,l,m) of Eqs. (9) and (10), once the previous order has been solved. A full list of the solved mapping and aberration coefficients (up to 5$^{th}$ order) are described in Supplement 1. Each linear equation set of order **o** relates to the surface coefficients $\bar{f}_{i,st}$ with s+t=**o**+1, while the mapping coefficients $\bar{u}_{\mathrm{I,jklm}}$, $\bar{v}_{\mathrm{I,jklm}}$ and aberration coefficients $\bar{\epsilon}_{x,\,\mathrm{jklm}}$, $\bar{\epsilon}_{y,\,\mathrm{jklm}}$ with j+k+l+m=**o**. Then we sort them in ascending order and get the liner equations by setting unwanted aberration coefficients to zero or by minimizing a combination thereof as required by the targeted specifications of the imaging freeform system. For each order, we apply the elimination method for solving linear systems to eliminate the unknown mapping coefficients and to obtain a reduced linear system that expresses the aberration coefficients as linear functions of the unknown surface coefficients of that order.

Note that the resulting linear equation system can be either squared, overdetermined or underdetermined. In all cases, we use the Moore-Penrose pseudoinverse (MATLAB's *pinv* function) to solve the linear equation set with a minimum-norm least-squares solution for the respective surface coefficients. If the least-squares solution is not obtained for an overdetermined linear system, we then define a basic set of weighting factors

Optics EXPRESS

$WF_{jklm} = (\mathrm{ENPD}/2)^{j+k}\left(\frac{FOV}{\sqrt{2}}\right)^{l+m}$ that is multiplied with the reduced linear equations of the same index (j,k,l,m). The weighted least-squares solution [37] for the reduced linear system then takes both the maximum entrance pupil diameter and largest FOV into account to simultaneously minimize all properly weighted aberrations for each order, and to calculate the corresponding surface and aberration coefficients. The calculated coefficients are now substituted into the original linear system to calculate the remaining unknown mapping coefficients of that order. Here, the weighted linear least-square solution is still exact and different from thee commonly used weighting factors in optical system optimization.

When a specified order is reached (typically up to 6th surface order s+t), the set of surface coefficients $\bar{f}_{i,st}$ is obtained in a deterministic way that fully describe the N reflective optical surfaces. In addition, the power series for the mapping and aberration functions enables a rapid function-based analytic ray tracing evaluation by accurately substituting the calculated mapping and aberration coefficients for all index combinations of j+k+l+m=1,2,3... up to the specified solution order. If needed, even higher ray tracing precision can be achieved by increasing the power series order.

In general, the deterministic 'first time right' calculation provides a quite good starting imaging system. The metrics to evaluate imaging performance and manufacturability are immediately available and given as introduced in the next section. All surfaces and system parameters can be exported to commercial optical design software for fine-tuning and double-check. Meanwhile, our built-in optimization tool (MATLAB's FMINSEARCH with bound constraint) can continue to improve the performance by varying the surface positions within certain ranges while minimizing the merit function of several selected metrics.

### 2.3. Evaluation and optimization metrics

After we obtained all the mapping coefficients $\bar{u}_{i,jklm}$, $\bar{v}_{i,jklm}$, surface coefficients $\bar{f}_{i,st}$ as well as aberration coefficients $\bar{\epsilon}_{x,\,jklm}$, $\bar{\epsilon}_{y,\,jklm}$ from the 'first time right' calculation, the metrics are essential for a thorough system evaluation and further optimization. Two kinds of metrics are built, the feasibility metrics (smallest enclosed volume, obscuration and freeform departures from BFS) and the image quality metrics (full-field RMS spot size and maximum distortion).

***System layout and volume.*** The freeform surface sag in local coordinate is immediately constructed by the given coefficients following Eq. (3a). Then, arbitrary points on the calculated freeform surfaces along x- and y-direction are sampled to form 3D point clouds, which are all converted to global coordinates, the conversion process is shown in the Supplement 1. We extract the point clouds over the x=0 plane and plot it to generate the 2D layout.

To calculate the packaging volume, we trace considerable 4D rays covering the full FOV and full entrance pupil, then the maximum and minimum values of all surfaces in global coordinates are determined as $X_{min}$, $X_{max}$, $Y_{min}$, $Y_{max}$ and $Z_{min}$, $Z_{max}$, respectively. The smallest enclosed volume metric is defined as the volume of the minimum box that can put the erect system inside with 5mm-margin (H × W × L) as seen in Fig. 3(**a**)

$$V_{3d} = (Z_{max} - Z_{min}) \times (Y_{max} - Y_{min}) \times (X_{max} - X_{min}). \tag{11}$$

***Obscuration.*** Obscuration happens very frequently during the design of off-axis mirror systems. Without intervention, an off-axis design is easily lost into impractical obscurations, which can be a substantial bottleneck to overcome. We have defined an obscuration metric as a penalty term for the merit function to address this problem [38]. The metric is universal to multi-mirror systems, e.g. three- or four-mirror systems.

To quantify the obscuration automatically, the generated 2D layout is numbered into sequential surface 1...N+2 and divided into different regions. One region is defined as two adjacent real surfaces (in solid lines) as well as the virtual in-between boundaries (in dotted lines). For

Optics EXPRESS

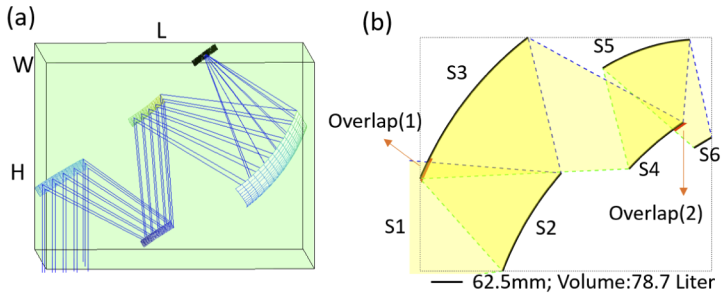


**Fig. 3.** Analytic metrics for performance evaluation and optimization. (a) The enclosed volume for packaging size. (b) The obscuration penalty metric is calculated as the sum of all the overlaps.

example, five regions are shown in Fig. 3(**b**). When mechanical holders are needed for mounting the optical components, margin zones with required values could be added to the clear aperture, which avoids the obscuration from the assembly. One overlap segment is detected once a third solid surface is intersected with a region, highlighted in orange lines. Traversing all the surfaces in one region i, all the overlaps are summed up as the overlap (i). By traversing all the regions, the obscuration metric is calculated as the sum of all the overlaps:

$$\text{obscuration} = \sum_{i=1}^{N-1} \text{overlap}(i). \tag{12}$$

***Freeform departure from best fitting sphere***. Small freeform departures from besting fitting sphere reduce the difficulty and cost in manufacturing freeform mirrors. Thus, we monitor and optimize this value for each surface to ensure good manufacturability. As the surface sag function is given, we obtain the best fitting sphere (BFS) radius $c_i$ by different algorithms, for example, the Fast Sphere Fit by Sumith YD [39]. Subtracting the spherical part from the surface function to obtain the freeform departure contour

$$\Delta f_i(x,y) = \sum_{s=0}^{S}\sum_{t=0}^{T} \bar{f}_{i,st} x^s y^t - \frac{c_i(x^2+y^2)}{1+\sqrt{1-c_i^2(x^2+y^2)}},\ i = 1\ldots N. \tag{13}$$

The maximum value among all freeform surface peak-valley (PV) departures is chosen as this metric during the optimization process.

***Root-mean-square spot size.*** Besides the system feasibility and manufacturability, the image quality needs to be evaluated. The root-mean-square (RMS) spot size and wavefront error are both comprehensive criteria that consider the superposition of primary and high-order aberrations. In this work, we mainly use RMS spot sizes as the image sharpness criterion. The RMS spot size is assessed over a full field of view based on a specified sampling strategy, such as cartesian sampling and polar sampling [32].

From Eqs. (5)–(6), we obtain the radial aberration for arbitrary ray from a specified field H

$$\epsilon(\mathrm{H}) = \sqrt{\epsilon_x^2(p_x,p_y,\mathrm{H}) + \epsilon_y^2(p_x,p_y,\mathrm{H})}, \quad \text{with } {p_x}^2 + {p_y}^2 \le 1. \tag{14}$$

where, H represents one normalized field ($h_x$, $h_y$) according to the FOV definition:

$$\begin{cases} \mathrm{H}:\ -1 \le h_x \le 1, -1 \le h_y \le 1, \text{ in rectangular FOV.} \\ \mathrm{H}:\ {h_x}^2 + {h_y}^2 \le 1, \text{ in circular FOV.} \end{cases} \tag{15}$$

Optics EXPRESS

We then perform the RMS calculation by traversing considerable rays in $p_x$ and $p_y$ by a polar sampling strategy with arms $n_a$ and rings $n_r$:

$$\mathrm{RMS(H)} = \sqrt{\frac{1}{n_a n_r}\left(\sum_{i=1}^{n_a}\sum_{j=1}^{n_r}\epsilon_x^2(p_{x,ij}, p_{y,ij}, \mathrm{H}) + \sum_{i=1}^{n_a}\sum_{j=1}^{n_r}\epsilon_y^2(p_{x,ij}, p_{y,ij}, \mathrm{H})\right)}. \quad (16)$$

The RMS spot size metric is calculated as the average RMS value over the selected fields. Weighting factors can be furthermore added to improve the image quality for specified fields if needed.

***Distortion***. Distortion is an image aberration that does not affect the image sharpness but causes image deformation. Current digital processing techniques provide good corrections, but in optical design there are typically minimum requirements. Following Eqs. (4)–(6), the distortion is calculated by the deviation of the chief ray ($p_x = 0, p_y = 0$) from the ideal image in percentage

$$\mathrm{DIST(H)} = \frac{\sqrt{\epsilon_x^2(0,0,\mathrm{H}) + \epsilon_y^2(0,0,\mathrm{H})}}{\sqrt{u_{ideal}^2(\mathrm{H}) + v_{ideal}^2(\mathrm{H})}} \times 100\%. \quad (17)$$

As the distortion is a function of fields, the distortion metric value is defined as the maximum distortion over the selected fields.

## 3. Results and discussion

Two freeform optical systems are designed using the proposed design framework. The first example highlights the capability of our method in handling fast F-number and wide FOV simultaneously that is typically lack in most four-mirror freeform imaging system designs. Secondly, we introduce a new kind of freeform imaging designs with 'double-pass surface' that provides huge potentials for super-compact, high-performing, cost-friendly imaging systems.

### 3.1. Four-mirror telescope design with fast f-number and wide FOV

Reflective imaging systems are well-known for their application in telescopes. One challenge for telescope design is to reach a large FOV, thus most such systems have an FOV of less than 10 degrees [15,31,40,41]. As the FOV increases, astigmatism and field curvature become quite difficult to correct. Another challenge is using a fast f-number that is typically required to ensure high spatial resolution; however, an unobscured, fast telescope can bring large high-order aberrations and lots of overlaps if the volume is also strictly constraint. Here, we identified a reference design with very challenging specifications as listed in Table 1 [42].

**Table 1. The specifications of first exemplary design**

| Specifications | Parameters |
|---|---|
| Focal Length (mm) | 250 |
| Field of view (°) | 25.5×8.5 |
| F-number | 2.5 |
| Enclosed volume(mm) | 70L |
| Wavelengths(μm) | 0.5-5 (2μm) |
| RMS spot diameter (μm) | < 18 |
| Distortion | < 4.5% |
| Telecentricity(°) | < 1 |

To begin with, the proposed design method shows clear advantages for packaging issues, since we can choose the five positions of initial planes to fulfill the physical size requirement.

Optics EXPRESS

We casually selected five points as the vertices of four mirrors and the image plane in global coordinate. To make the on-axis chief ray exactly go through these points, the tilt angle for each surface is calculated. Thus, the layout is determined as shown in Fig. 4(a), which is a classic zigzag four-reflection system. The focal lengths for x and y dimensions are identical as 250mm with the aperture stop on M3. Variable stops on other mirror have been tried while M3 provides the smallest size.

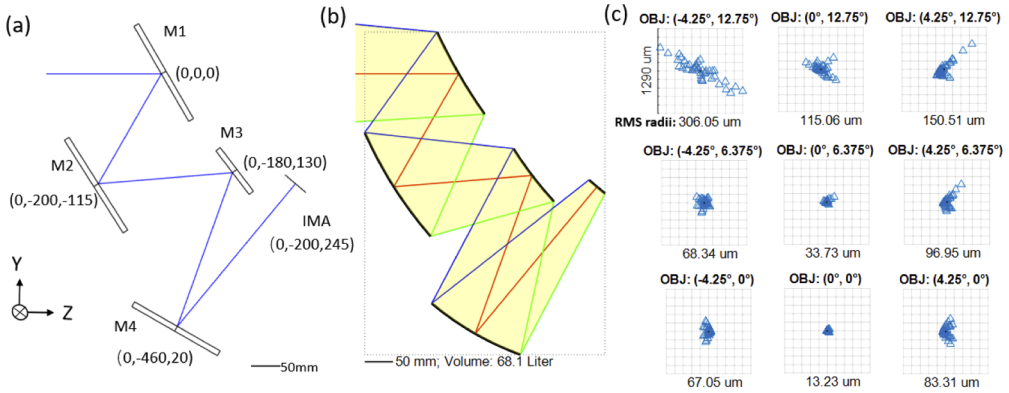


**Fig. 4.** The large FOV, fast four-mirror design example. (a) Global coordinate of initial planes. (b) The cross-section 2D layout after a 'first time right' calculation. (c) Spot diagram for nine selected fields with corresponding RMS radii values.

With all system specifications and surface positions known, we can derive two sets of differential equations to fully describe the system parameters, as described in Eqs. (9) and (10). The corresponding optical path lengths are determined by arbitrary points on mirrors $(u_i, v_i, f_i)$ or on detector $(u_5, v_5, z_D)$, according to Eqs. (7) and (8). Note that these points are in local coordinate, we need to calculate the distances in global coordinates by multiplying a constant conversion matrix as explained in Supplement 1. The subsequent calculation process to solve these two differential equation sets is initiated as in Sec. 2.2. Here, more details for this design are described.

(1) We evaluate Eqs. (9) and (10) for all j + k + l + m = 1 and i = 1 . . . 4, which results in 16 nonlinear equations with 24 unknowns. Setting the four first-order ray aberration coefficients $\bar{\epsilon}_{x,\,1,0,0,0}, \bar{\epsilon}_{x,\,0,0,1,0}, \bar{\epsilon}_{y,\,0,1,0,0}, \bar{\epsilon}_{y,\,0,0,0,1}$ to zero leaves 12 mapping coefficients $\bar{u}_{i,1,0,0,0}$, $\bar{u}_{i,0,0,1,0}$, $\bar{v}_{i,0,1,0,0}$, $\bar{v}_{i,0,0,0,1}$ (i = 2,3,4) and 8 second-order surface coefficients $\overline{f}_{i,st}$ (s + t = 2, i = 1 . . . 4) as unknowns. We further define four parameters $c_{i,xy}$ that allows different second-order coefficients in x- and y-direction of the respective mirrors which are used later for optimization, that is $\overline{f}_{i,0,2} = c_{i,xy} . \overline{f}_{i,2,0}$, and the values of $c_{i,xy}$ $(i = 1 \ldots 4)$ have been set to 1 initially. Now, we can solve these 20 nonlinear equations with 20 unknowns using MATLAB function *fsolve*.

(2) For each higher order j+k+l+m=2,3. . . , we continue to derive the differential equations sequentially, until the surface coefficients reach 6$^{th}$ order, and the mapping and aberration coefficients have 5$^{th}$ order. These calculations result in 52 surface coefficients, 375 mapping and 125 aberration coefficients. The whole list of the calculated mapping and aberration coefficient terms is given in Supplement 1. Note that several of the mapping and aberration coefficients are interdependent.

The result of this initial calculation is shown in Fig. 4(b). Here, the obscuration has been totally removed by adjusting the mirror positions, and the following optimization process maintains the

Optics EXPRESS

zero-obscuration condition. The corresponding RMS spot diagram of nine selected fields (three equal-spacing fields in X: -4.25°, 0°, 4.25° and +Y: 0°, 6.375°, 12.75° given XZ-plane symmetry) is shown in Fig. 4(c). As we can see, the RMS spot radius of on-axis field is already as small as 13.23μm while the maximum field has an RMS spot radius of 306.05μm. The maximum distortion (about 6.6%) and freeform PV departure (about 3343 μm) are not controlled in the beginning. At this step, we have quickly reached a reasonable first layout with zero obscuration while keeping an acceptable performance.

To further improve the imaging performance while keeping a feasible layout and moderate manufacturability, the metrics of obscuration, distortion, full-field RMS spot sizes, maximum freeform PV departure and smallest enclosed volume are added to the integrated merit function. The maximum distortion is set to be less than 4.5%. The volume is bounded to be within 70L, and the maximum telecentricity angle is desired to be lower than 1° to form a good uniform illuminance. The maximum freeform departure is set to be within reasonable manufacturing limits (PV < 500μm) [43]. The variables are the positions of all surface vertices, fluctuating within certain ranges, e.g. ±10mm, as well as four second-order surface coefficients $c_{i,xy}$.

After a 500-iteration optimization which takes less than five minutes, both the image quality and the fabrication related metrics have been clearly improved. As seen in Fig. 5(a), the cross-section 2D layout is not far away from the initial design with volume less than 70L, and the maximum freeform PV departures is 254μm. Figure 5(b) shows the RMS spot radii has dropped about 10 times with average value 16.9μm, particularly the central field has an RMS spot radius of 1.07μm, far below the Airy Radius 6μm at central wavelength 2μm (black circles). Here, the RMS spot results are evaluated from Zemax raytracing by importing the calculated coefficients (no optimization) as it is more familiar to the optical design community, although the built-in analytic raytracing gives quite similar results.

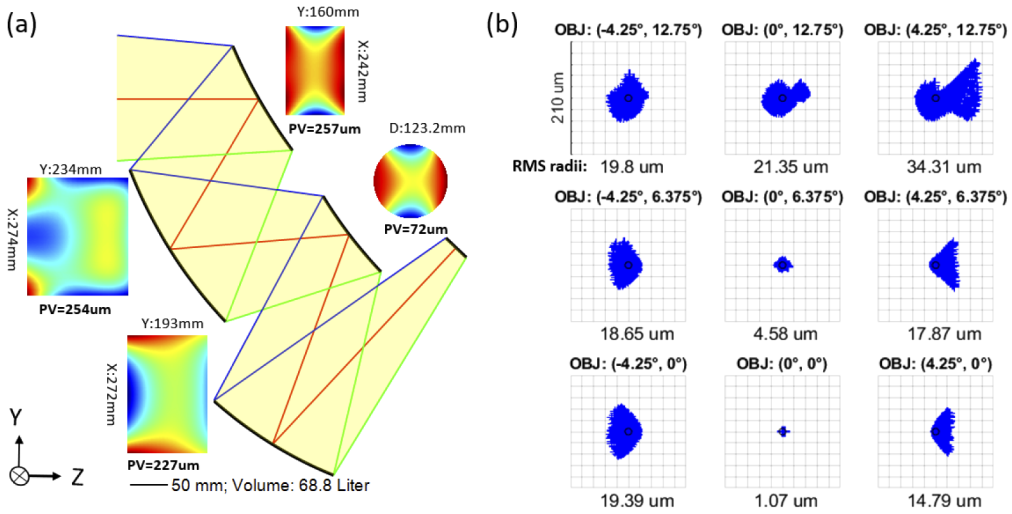


**Fig. 5.** Optimization results of four-mirror freeform telescope design with volume < 70L (a) Cross-section 2D layout with peak-to-valley freeform departures (PV) from the base sphere for each mirror. (b) Spot diagram for nine selected fields with corresponding RMS radii values.

In circumstances where system volume is not strictly constraint, the imaging performance can be further improved. As distortion is easier to be corrected by digital image processing technique afterwards, this value could be loosened if otherwise the image quality must be compromised. We have loosened the volume to 80L and maximum distortion to 6%. The same optimization settings have been used, and the subsequential results are shown in Fig. 6(a) and 6(b). The image qualify

Optics EXPRESS

in terms of spot diagram is enhanced from 16.9μm to 7.33μm. The freeform PV departures are slightly worse but still less than 500 μm, achieving an excellent result in comparison with the reference design's 1053μm [42]. The telecentricity is lower than 1 degree for all selected fields.

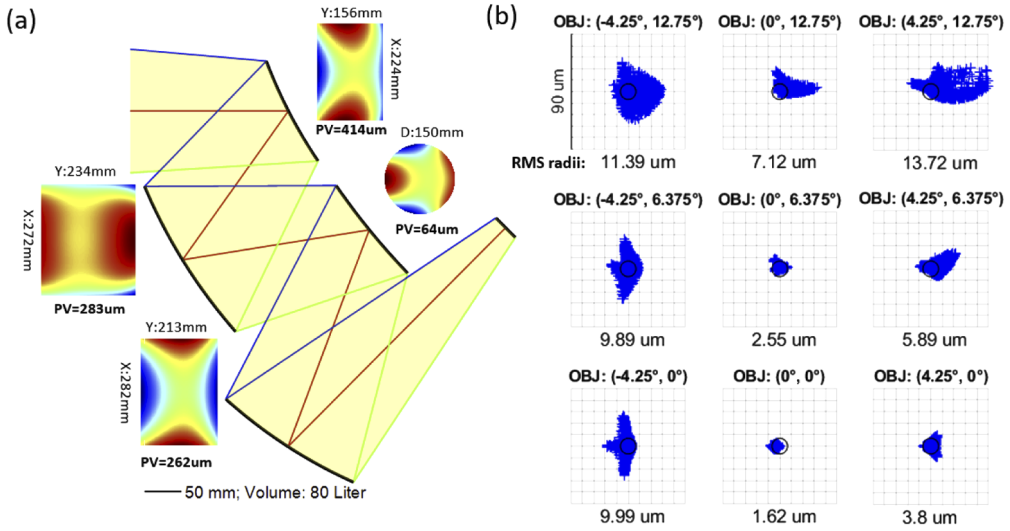


**Fig. 6.** Subsequent optimized results with volume <80L (a) Cross-section layout with PV freeform departures. (b) Spot diagram for nine selected fields with corresponding RMS radii values.

As a summary, the design algorithm has shown excellent capability in achieving large FOV, fast f-number telescope design with reduced input parameters. Anyone with basic optical design knowledge should be able to perform the design. Note that, the above optimization process is based on a multidimensional unconstrained nonlinear minimization method (Nelder-Mead direct search method in MATLAB *fminsearch*). Any other suitable optimizer or a commercial software with built-in advanced optimizer can be used to perform this optimization task, e.g. Zemax or code V. Regarding this design, we performed further optimization in Zemax, and a diffraction-limited performance is possible while the freeform PV departure, telecentricity and volume size are not constraint.

### 3.2. *Two-freeform, three-mirror, four-reflection design*

In spite of faster F-numbers and larger FOVs, freeform four-mirror designs bring in extra complexity to both mirror fabrication and system assembly compared to its three-mirror counterpart designs. As a promising alternative, we have investigated a new type of multi-reflection mirror systems **where at least one of the mirrors is passed twice in the ray path with desired overlap** (not mutually centered to provide more flexible designs). This general idea was proposed over forty years ago by Dave Shafer [44] and we have implemented it in our design framework, which is the first time among current direct design methods to our knowledge. It is important to distinguish this concept from designs where two mirrors share the same substrate without desired overlap in their footprints [45].

Recently, we noticed that curved image sensor has been used in a three-freeform-mirror design (TFM) to greatly improve the imaging performance [40]. Both Legendre and Zernike polynomial surface expressions have been explored with the design specifications listed in Table 2. It is well-known that curved sensors can compensate field curvature to ensure a sharp image [46–48], but it can be a double-edged sword since they are still costly and not widely fabricated. Here, we demonstrate that the proposed method can offer a new class of freeform designs with 'double-pass

Optics EXPRESS

surface' strategy, which not only maintains a comparable image quality but also keeps a flat sensor for the challenging specifications.

**Table 2. The specifications of second exemplary design**

| Specifications | Parameters |
|---|---|
| Focal Length (mm) | 250 |
| Field of view (°) | 7.2×7.2 |
| F-number | 2.5 |
| Wavelengths(μm) | Visible (0.587μm) |
| RMS spot size (μm) [a] | < 5 |
| Distortion | < 1.33% |

[a]The results were achieved by using a toroidal sensor. If a flat sensor is used, the design has a much larger RMS spot radius (typically >20 μm).

Regarding the four-reflection cases, there are three possibilities to generate the "double-pass surface", respectively M1/3, M1/4 and M2/4. Several showcases of each type have been calculated by the proposed method, as seen in Fig. 7. It is worthy to point out Fig. 7(a) shows a fabrication-friendly design by using only two surfaces (one freeform and one spherical). We select these ones for their high feasibility in mirror/detector positioning and potential good image quality. From a general impression of playing with this new class, M1/M3 option has the largest amount of reasonable designs, while M1/4 ones are typically quite large and bizarre and M2/4 ones have narrow space for detector. Note that, this statement might be not suitable for undiscovered special cases. To further ease the fabrication, we always define the "double-pass surface" as a spherical surface.

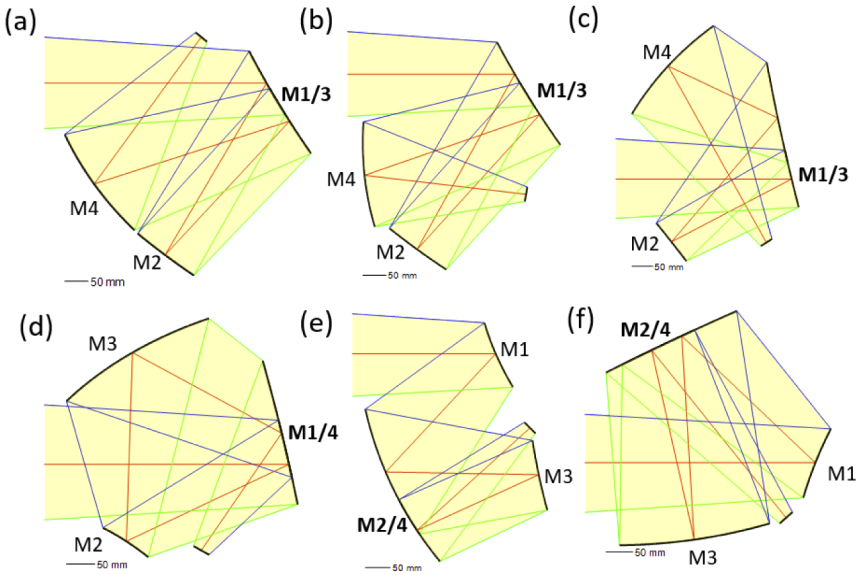


**Fig. 7.** The proposed freeform optical design method unlocks a new class of three-mirror, four-reflection freeform systems with three different 'double-pass surface' options. (a)-(c) M1/M3. (d) M1/M4. (e)-(f) M2/M4. Note all the layouts are based on real raytracing with the design parameters for visualization: focal length 250mm, F/2.5, FOV 7.2°×7.2°.

Optics EXPRESS

Among all, one M2/M4 case shows the highest potentials for compactness and image quality. We select this one to continue the design following the specifications in Table 2. To start the design process, the input parameters should be defined to initialize an original geometry, the second option of surface distances plus tilts is used. Details on the coordinate conversions are in Supplement 1. As the process has been introduced in previous sections, here we only emphasize the altered implementations to address the double-pass strategy.

(1) We evaluate the first order equations that result in a nonlinear system of 16 non-vanishing equations. Setting the four first-order ray aberration coefficients to zero leaves 12 mapping coefficients and 4 second-order surface coefficients as unknowns, that is $f_{i,2,0}, f_{i,0,2}$ $(i = 1, 3)$, whereas the base curvature $f_{2,0,2} = f_{2,2,0}$ at the joint mirror is one extra pre-defined parameter like the surface distances/tilts which could be optimized later. The nonlinear system is thereon ready to be solved.

(2) We calculate the surface coefficients up to $6^{\text{th}}$ order for the surfaces and up to $8^{\text{th}}$ order for the mapping and aberration coefficients while keeping the joint mirror strictly spherical.

With the surface positions and the altered implementations known, we perform the "first time right" calculation and the built-in optimization process. The selected metrics are the smallest RMS spot radii for nine fields, zero distortion, maximum distortion < 2%, volume < 24L and freeform PV departures < 500μm. This optimization allows the predefined surface positions and the spherical surface M2/M4 radius to change within a certain range. After 100-iteration optimization (about 76 seconds), the cross-section 2D layout is shown in Fig. 8(a), with a volume of 23.7L and two freeform PV departures 427μm and 278μm respectively. The spot diagram in Fig. 8(b) shows a moderate-corrected system, where the maximum RMS spot radius is 9.5 μm and the minimum RMS spot radius is 1.9 μm. Here, we noticed that the on-axis field is much better corrected than other fields, like in most of our designs. Given that the "first time right" calculation puts many priorities on spherical and comatic aberration corrections despite their orders, and the optimizer is also based on this setting, therefore on-axis field usually has a much better performance than others.

To verify the calculated design and realize a more balanced image quality, we exported all three surfaces into Zemax, and a further optimization is performed to tweak the design. We used the default merit function: RMS spot x+y referring to chief ray, pupil integration over 16 rings and 12 arms. DIMX is added to control distortion over different fields, as well as the maximum aspheric sag to allow PV departures from BFS less than 500 μm. The working f-number (WFNO) is set to be 2.5 and the entrance pupil 100 mm ensure an effective focal length of 250 mm. All surface positions are frozen to keep the zero-obscuration layout, only the coefficients of the two freeform surfaces plus the one spherical radius are set as variables. After about five-minute optimization, the merit function value stopped decreasing. The final 2D layout of the system with a volume of 25.3L is shown in Fig. 9(a), where the freeform PV deviations of M1 and M3 are slightly decreased to 419μm and 230μm induced by increased optical powers and larger sizes. Note that the freeform departure contours are similar to those generated by the "first time right" result in Fig. 8(a), implying the capability of the proposed method in finding an excellent initial solution. The imaging performance in terms of RMS spot radii is shown in Fig. 9(b), where the maximum RMS spot radius is 4.7μm and minimum RMS spot radius is 2.7μm. Distortion seems to be difficult to be further corrected without compromising the image quality. As the location of stop is only feasible on M1 and M3, thus the configuration has lost certain symmetry over the stop, which causes a slightly worse distortion (2%) correction in comparison to the reference three-mirror system [40] (1.33%). However, the distortion is still negligible or easily corrected by using digital processing, thus we consider it as a reasonable value.

Critical metrics are compared with the reference designs [40], in terms of volume, RMS spot size, distortion, freeform PV departure and sensor shapes as summarized in Table 3. Since the

Optics EXPRESS

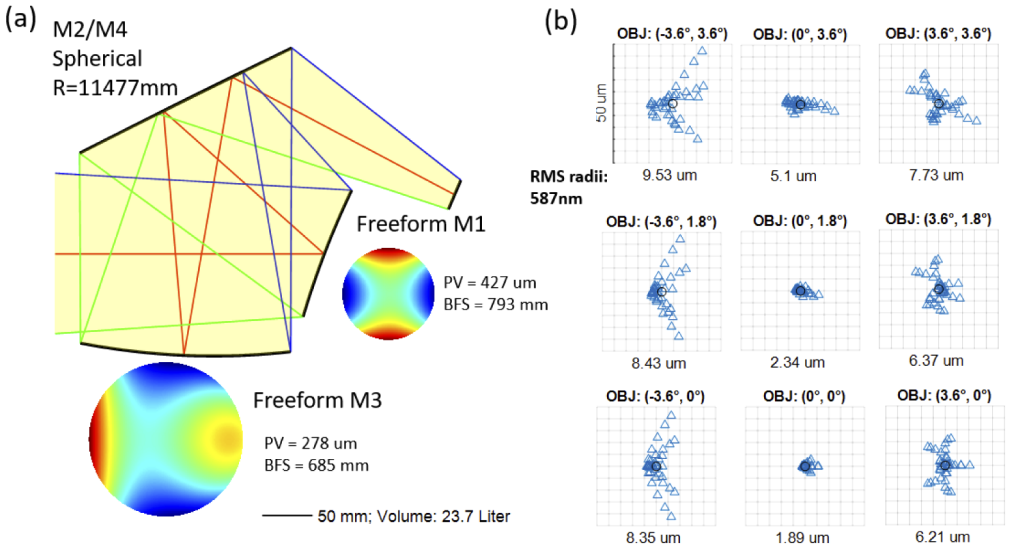


**Fig. 8.** Optimization results of the two-freeform, three-mirror four-reflection design with volume < 24L. (a) Cross-section 2D layout with 23.7L volume and the peak-to-valley freeform departures (PV) of M1 and M3 from the best fitting sphere (BFS) 427μm and 278μm respectively. (b) Spot diagram for nine selected fields with corresponding RMS radii values.

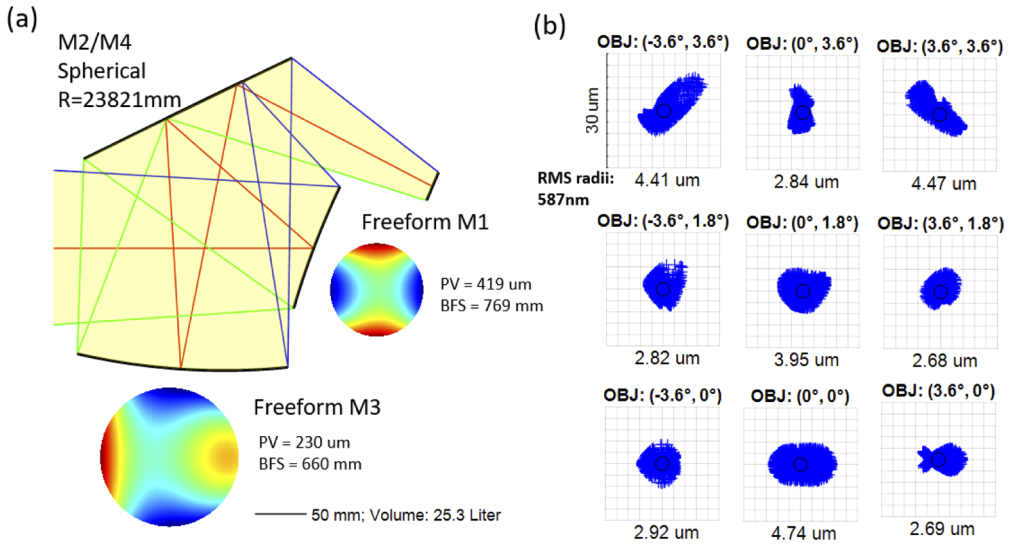


**Fig. 9.** Subsequent optimized results in Zemax with fixed surface positions and various weights for fields. (a) Cross-section 2D layout with 25.3L volume and the PV freeform departures of M1 and M3. (b) Balanced spot diagram for nine selected fields with corresponding RMS radii values

Optics EXPRESS

focal length, FOV, F# and the wavelengths are the same as in Table 2, so these values are not listed. The volume is reduced by almost 50%. As for feasibility, we use two freeform mirrors in comparison to three freeform mirrors as in the counterpart designs, while the maximum freeform PV departure value is about 60% less, demonstrating a potential lower cost on the component fabrication and alignment. Besides, we use a flat image plane while the reference designs have a toroid CMOS sensor to compensate for field curvature. As for image quality, the average spot radii for nine selected fields indicates an equal performance, and the distortion is slightly worse which is insignificant and can be corrected by digital processing if needed.

**Table 3. The comparison of image quality and manufacturability**

| Specifications | | Ref. Design 1 [40] | Ref. Design 2 [40] | Our design |
|---|---|---|---|---|
| Surface type | | Legendre | Zernike | XY polynomial |
| Volume (liter) | | 49.1 | 47.2 | **25.3** |
| RMS spot radius (μm) | Max | 1.4 | 5.8 | 2.7 |
| | Min | 5.9 | 9.1 | 4.7 |
| | Mean | 3.7 | 7.7 | < **3.7** |
| Distortion | | < 1.33% | < 1.38% | 2% |
| Freeform PV departure from BFS (μm) | | M1:105.5 | M1:128.1 | M1: **419** |
| | | M2:1098.9 | M2:1053.4 | M2: spherical |
| | | M3:354.9 | M3:298.2 | M3: 230 |
| Sensor Shape | | Toroid | Toroid | **Flat** |

As a short summary, the established two-freeform, three-mirror, four-reflection designs have been proven to be high-performing and super compact, opening up a largely extended design space to explore and seek competitive solutions for existing multi-reflection designs. However, it is important to distinguish our 'double-pass' design cases from the well-known Offner designs in literature where two individual mirrors share separate parts (no overlap) of a joint substrate [49].

## 4. Conclusions

In this work, we presented a freeform optical design framework based on generalized differentiable ray tracing and simultaneous multi-surface "first-time right" analytic calculations. Consequently, the proposed method is beneficial for both novice and experienced optical designers as it requires only basic optical design knowledge. Particularly, the optimizer in this work is just a basic tool, and any other more advanced optimization algorithms can be used on top of the generalized ray tracing strategy and "first time right" calculations. We demonstrated the capabilities of our method on two challenging design problems. Firstly, we designed a wide FOV ($8.5° \times 25.5°$), fast f-number (F2.5) telescope with four freeform mirrors. With the established metrics such as enclosed volume, obscuration, freeform PV departures to indicate feasibility as well as the RMS spot radius, distortion to represent image quality, we gained very flexible control over the optimization process, and achieved high performance. In the second design, we unlocked a new series of freeform imaging systems with "double-pass surface" strategy, which provides many more design degrees of freedom to fold optical path without increasing the component number. When compared with corresponding three-freeform-mirror imaging designs, our design shows comparable image quality with a more compact volume (reduced by 50%), a highly cost-friendly consideration with smaller freeform PV departure (60% less) and less freeform components.

Without loss of generality, our "first time right" method can be applied to imaging system designs with a flexible number of mirrors and/or lenses. Compared to the time-consuming, intensive optimization-based methods as in commercial optical design software, the freeform

Optics EXPRESS

surface coefficients are analytically calculated in our method, and each calculation can give a "first time right" design within the solution space of the given system geometry. Thus, the optimization process is only used for searching a better system geometry, e.g. surface positions and tilts, not for optimizing the freeform surface coefficients. Its core strength lies in the rapid generation of initial design solutions with already significantly improved imaging performance while requiring a largely reduced input parameter space. Note that one single "first time right" calculation takes only dozens of milliseconds, it is very fast to automatically generate large quantities of feasible starting designs for screening, therefore it can be performed as a global searching method. In general, a feasible design takes about five minutes, including a 500-loop optimization to find a local minimum from varying the input parameters for "first time right" calculations and subsequently evaluating the selected metrics. Due to the rapid speed, it is possible to investigate numerous starting geometries in a short time with the provided metrics to find the optimal geometry for different mirror systems. Furthermore, with reduced input parameter space and the deterministic output, the proposed framework is suitable for optical designers in all experience levels who are interested in exploring new layouts and design solutions.

As such, the presented design framework has the full potential to provide a thorough and fast solution space search for a wide range of applications. Throughout the development of these two examples, we have evaluated various geometries and found that the initial geometry played a very critical role in achieving an optimal off-axis freeform imaging system. Future work will include applying more advanced optimization algorithms to enable a further automated global search.

**Funding.** Fonds Wetenschappelijk Onderzoek (12C9817N, G044516N); Vrije Universiteit Brussel (Hercules, Methusalem, OZR); H2020 Future and Emerging Technologies (FET-OPEN No.829104, SensApp).

**Acknowledgments.** We thank Vrije Universiteit Brussel for providing necessary equipment and software licenses.

**Disclosures.** The authors declare no conflict of interest.

**Data availability.** The authors confirm that the data supporting the findings of this study are available within the article and its supplementary materials.

**Supplemental document.** See Supplement 1 for supporting content.

## References

1. J. Li, P. Fejes, D. Lorenser, B. C. Quirk, P. B. Noble, R. W. Kirk, A. Orth, F. M. Wood, B. C. Gibson, and D. D. Sampson, "Two-photon polymerisation 3D printed freeform micro-optics for optical coherence tomography fibre probes," Sci. Rep. **8**(1), 14789 (2018).
2. T. Gissibl, S. Thiele, A. Herkommer, and H. Giessen, "Sub-micrometre accurate free-form optics by three-dimensional printing on single-mode fibres," Nat. Commun. **7**(1), 11763 (2016).
3. Z. Hong and R. Liang, "IR-laser assisted additive freeform optics manufacturing," Sci. Rep. **7**(1), 1–7 (2017).
4. W. Jahn, M. Ferrari, and E. Hugot, "Innovative focal plane design for large space telescope using freeform mirrors," Optica **4**(10), 1188–1195 (2017).
5. J. Volatier and G. Druart, "Differential method for freeform optics applied to two-mirror off-axis telescope design," Opt. Lett. **44**(5), 1174–1177 (2019).
6. J. Reimers, A. Bauer, K. P. Thompson, and J. P. Rolland, "Freeform spectrometer enabling increased compactness," Light: Sci. Appl. **6**(7), e17026 (2017).
7. H. Huang and H. Hua, "High-performance integral-imaging-based light field augmented reality display using freeform optics," Opt. Express **26**(13), 17578–17590 (2018).
8. S. Schmidt, S. Thiele, A. Toulouse, C. Bösel, T. Tiess, A. Herkommer, H. Gross, and H. Giessen, "Tailored micro-optical freeform holograms for integrated complex beam shaping," Optica **7**(10), 1279–1286 (2020).
9. R. Wu, Z. Feng, Z. Zheng, R. Liang, P. Benítez, J. C. Miñano, and F. Duerr, "Design of Freeform Illumination Optics," Laser Photonics Rev. **12**(7), 1700310 (2018).
10. R. Wu, L. Yang, Z. Ding, L. Zhao, D. Wang, K. Li, F. Wu, Y. Li, Z. Zheng, and X. Liu, "Precise light control in highly tilted geometry by freeform illumination optics," Opt. Lett. **44**(11), 2887–2890 (2019).
11. J. P. Rolland, M. A. Davies, T. J. Suleski, C. Evans, A. Bauer, J. C. Lambropoulos, and K. Falaggis, "Freeform optics for imaging," Optica **8**(2), 161–176 (2021).
12. Y. Nie, H. Gross, Y. Zhong, and F. Duerr, "Freeform optical design for a nonscanning corneal imaging system with a convexly curved image," Appl. Opt. **56**(20), 5630–5638 (2017).
13. A. Bauer, E. M. Schiesser, and J. P. Rolland, "Starting geometry creation and design method for freeform optics," Nat. Commun. **9**(1), 1756 (2018).

Optics EXPRESS


14. Y. Zhong and H. Gross, "Initial system design method for non-rotationally symmetric systems based on Gaussian brackets and Nodal aberration theory," Opt. Express **25**(9), 10016–10030 (2017).
15. T. Yang, G. Jin, and J. Zhu, "Automated design of freeform imaging systems," Light: Sci. Appl. **6**(10), e17081 (2017).
16. T. Yang, D. Cheng, and Y. Wang, "Direct generation of starting points for freeform off-axis three-mirror imaging system design using neural network based deep-learning," Opt. Express **27**(12), 17228–17238 (2019).
17. J. C. Miñano, P. Benítez, and B. Narasimhan, "Freeform aplanatic systems as a limiting case of SMS," Opt. Express **24**(12), 13173–13178 (2016).
18. J. C. Minano, P. Benitez, W. Lin, J. Infante, F. Munoz, and A. Santamaria, "An application of the SMS method for imaging designs," Opt. Express **17**(26), 24036–24044 (2009).
19. Y. Nie, H. Thienpont, and F. Duerr, "Multi fields direct design approach in 3D calculating a two surface freeform lens with an entrance pupil for line imaging systems," Opt. Express **23**(26), 34042–34054 (2015).
20. G. W. Forbes, "Fitting freeform shapes with orthogonal bases," Opt. Express **21**(16), 19061–19081 (2013).
21. A. Yabe, "Representation of freeform surfaces suitable for optimization," Appl. Opt. **51**(15), 3054–3058 (2012).
22. K. Fuerschbach, J. P. Rolland, and K. P. Thompson, "Extending Nodal Aberration Theory to include mount-induced aberrations with application to freeform surfaces," Opt. Express **20**(18), 20139–20155 (2012).
23. K. Thompson, "Description of the third-order optical aberrations of near-circular pupil optical systems without symmetry," J. Opt. Soc. Am. A **22**(7), 1389–1401 (2005).
24. P. Benitez, M. Nikolic, and J. C. Miñano, "Analytical solution of an afocal two freeform mirror design problem," Opt. Express **25**(4), 4155–4161 (2017).
25. F. Duerr, P. Benítez, J. C. Miñano, Y. Meuret, and H. Thienpont, "Analytic free-form lens design in 3D: coupling three ray sets using two lens surfaces," Opt. Express **20**(10), 10839–10846 (2012).
26. Y. Nie, R. Mohedano, P. Benítez, J. Chaves, J. C. Miñano, H. Thienpont, and F. Duerr, "Multifield direct design method for ultrashort throw ratio projection optics with two tailored mirrors," Appl. Opt. **55**(14), 3794–3800 (2016).
27. D. R. Shafer, "Four-mirror unobscured anastigmatic telescopes with all-spherical surfaces," Appl. Opt. **17**(7), 1072–1074 (1978).
28. J. M. Sasian, "Flat-Field, Anastigmatic, Four-Mirror Optical System for Large Telescopes," Opt. Eng. **26**(12), 261297 (1987).
29. A. Rakich, "Four-mirror anastigmats, part 1: a complete solution set for all-spherical telescopic systems," Opt. Eng. **46**(10), 103001 (2007).
30. J. M. Howard and B. D. Stone, "Imaging with four spherical mirrors," Appl. Opt. **39**(19), 3232–3242 (2000).
31. J. C. Papa, J. M. Howard, and J. P. Rolland, "Starting point designs for freeform four-mirror systems," Opt. Eng. **57**(10), 1–11 (2018).
32. G. W. Forbes, "Optical system assessment for design: numerical ray tracing in the Gaussian pupil," J. Opt. Soc. Am. A **5**(11), 1943–1956 (1988).
33. B. Said-Houari, "Power Series Solution," in *Differential Equations: Methods and Applications*, B. Said-Houari, ed. (Springer, 2015), pp. 125–140.
34. F. Duerr, Y. Meuret, and H. Thienpont, "Tracking integration in concentrating photovoltaics using laterally moving optics," Opt. Express **19**(S3), A207–A218 (2011).
35. F. Duerr, Y. Meuret, and H. Thienpont, "Potential benefits of free-form optics in on-axis imaging applications with high aspect ratio," Opt. Express **21**(25), 31072–31081 (2013).
36. F. Duerr and H. Thienpont, "Freeform imaging systems: Fermat's principle unlocks 'first time right' design," Light: Sci. Appl. **10**(1), 95 (2021).
37. C. L. Lawson and R. J. Hanson, *Solving least squares problems* (SIAM, 1995).
38. Y. Nie, F. Duerr, and H. Ottevaere, "Automated design of unobscured four-mirror freeform imaging systems," in *Optical Design and Fabrication 2019 (Freeform, OFT)* (OSA, Washington, DC, 2019), pp. M3B–M5B.
39. S. Yd, "Fast Sphere Fit [Non Iterative]," Preprint at https://www.mathworks.com/matlabcentral/fileexchange/51140-fast-sphere-fit-non-iterative (2020).
40. E. Muslimov, E. Hugot, W. Jahn, S. Vives, M. Ferrari, B. Chambion, D. Henry, and C. Gaschet, "Combining freeform optics and curved detectors for wide field imaging: a polynomial approach over squared aperture," Opt. Express **25**(13), 14598–14610 (2017).
41. C. Xu, X. Lai, D. Cheng, Y. Wang, and K. Wu, "Automatic optical path configuration variation in off-axis mirror system design," Opt. Express **27**(11), 15251–15261 (2019).
42. J. P. McGuire, "A Fast, Four-Mirror, Free-Form, Wide Field of View, Telecentric Telescope," in *Renewable Energy and the Environment* (OSA, Tucson, Arizona, 2013), pp. T3B–T6B.
43. B. Braunecker, R. Hentschel, and H. J. Tiziani, *Advanced optics using aspherical elements* (SPIE, 2008).
44. D. R. Shafer, "Anastigmatic two-mirror telescopes: some new types," Appl. Opt. **16**(5), 1178–1180 (1977).
45. T. Yang, J. Zhu, and G. Jin, "Compact freeform off-axis three-mirror imaging system based on the integration of primary and tertiary mirrors on one single surface," Chin. Opt. Lett. **14**(6), 060801 (2016).
46. B. Guenter, N. Joshi, R. Stoakley, A. Keefe, K. Geary, R. Freeman, J. Hundley, P. Patterson, D. Hammon, G. Herrera, E. Sherman, A. Nowak, R. Schubert, P. Brewer, L. Yang, R. Mott, and G. McKnight, "Highly curved image sensors: a practical approach for improved optical performance," Opt. Express **25**(12), 13010–13023 (2017).

Optics EXPRESS

47. S. Rim, P. B. Catrysse, R. Dinyari, K. Huang, and P. Peumans, "The optical advantages of curved focal plane arrays," Opt. Express **16**(7), 4965–4971 (2008).
48. D. Reshidko and J. Sasian, "Optical analysis of miniature lenses with curved imaging surfaces," Appl. Opt. **54**(28), E216–E223 (2015).
49. S. H. Kim, H. J. Kong, J. U. Lee, J. H. Lee, and J. H. Lee, "Design and construction of an Offner spectrometer based on geometrical analysis of ring fields," Rev. Sci. Instrum. **85**(8), 083108 (2014).